

# The benefit of thresholding carbon layers in electron tomographic tilt series by intensity downshifting

LIONEL C. GONTARD\*, JESÚS CINTAS† & RAFAL E. DUNIN BORKOWSKI‡

\*Departamento de Ciencia de los Materiales e Ingeniería Metalúrgica y Química Inorgánica, Universidad de Cádiz, Puerto Real, Spain

†Servicio de Microscopía Centro de Investigación, Tecnología e Innovación (CITIUS), Universidad de Sevilla, Sevilla, Spain

‡Ernst Ruska-Centre for Microscopy and Spectroscopy with Electrons and Peter Grünberg Institute, Jülich, Germany

**Key words.** Carbon layers, electron tomography, image processing, tomogram segmentation, intensity downshifting.

## Summary

When performing electron tomography, tilt series of images are often acquired from samples that contain unwanted carbonaceous material, such as an embedding resin, a thin carbon support film or hydrocarbon contamination. The presence of such layers can introduce artefacts in reconstructions, obscuring features of interest. Here, we illustrate the benefit of preprocessing a high-angle annular dark-field tomographic tilt series by thresholding unwanted low-density materials using a simple intensity downshifting procedure. The resulting tomograms have fewer artefacts and segmentation can be performed more accurately. We present two representative examples taken from studies of catalyst nanoparticles and amyloid plaque core material from the human brain.

## Introduction

Electron tomography is a powerful technique for obtaining three-dimensional (3D) information about the shape, density or composition of a specimen from a tilt series of images recorded in a transmission electron microscope (TEM). The reconstruction of an electron tomogram is often followed by manual or semi-automatic segmentation (Volkman, 2010). However, many samples contain significant amounts of low-density carbonaceous material, which can form the embedding material or form the thin support film. In some cases, the support film is itself of interest (e.g. Gontard *et al.*, 2008; González *et al.*, 2009; Leschner *et al.*, 2010; Grothausmann *et al.*, 2011), whereas in other cases the support should ideally be 'transparent' (Grimm *et al.*, 1998; Gontard *et al.*, 2014). Exposure to the electron beam can also result in the formation of regions of carbon-rich polymerized hydrocarbon contami-

nation, whose growth rate is approximately proportional to current density and irradiation time (Reimer & Kohl, 2008).

An electron tomographic reconstruction should ideally contain a discrete number of intensities, corresponding to the different material phases that are present in the sample. However, experimental results are often degraded by the use of a finite tilt increment and an incomplete tilt range (resulting in a 'missing wedge' of information in Fourier space), as well as by other artefacts that blur the borders between material phases, such as nonmonotonicity of the signal with specimen thickness due to the effects of dynamical diffraction and the presence of low-density material around the region of interest (Crowther *et al.*, 1970; Koster *et al.*, 2000; Midgley & Weyland, 2003; Fernández *et al.*, 2006; Midgley & Dunin-Borkowski, 2009; Van Den Broek *et al.*, 2012).

In materials science, an increasing number of methods is now applied during a workflow to improve the quality of a tomographic reconstruction, including the use of:

- i. specific acquisition methods such as dual-axis electron tomography (Tong *et al.*, 2006), full rotation specimen holders, focused ion beam milled specimens (Jarausch *et al.*, 2009) and impregnation methods (Gontard *et al.*, 2014);
- ii. preprocessing to enhance and discretise image intensities, improve the alignment of a tomographic tilt series or perform sinogram enhancement (Batenburg *et al.*, 2009; Ortolan *et al.*, 2009; Cao *et al.*, 2010; Volkman 2010; Bals *et al.*, 2011; Roelandts *et al.*, 2012; Scott *et al.*, 2012; Gontard, 2015);
- iii. reconstruction algorithms that are faster and result in fewer missing wedge artefacts (Jinschek *et al.*, 2008; Leschner *et al.*, 2010; Lange *et al.*, 2011; Goris *et al.*, 2012; Roelandts *et al.*, 2012; Alpers *et al.*, 2013; Leary *et al.*, 2013; Van den Broek *et al.*, 2014);
- iv. postprocessing of tomograms using approaches such as noise reduction (Frangakis *et al.*, 2001; Fernández

Correspondence to: Lionel C. Gontard, Departamento de Ciencia de los Materiales e Ingeniería Metalúrgica y Química Inorgánica, Universidad de Cádiz, Puerto Real 11510, Spain. Tel: +34 954489576; e-mail: lionelcg@gmail.com; web: www.lcgontard.es

& Li, 2009), thresholding, segmentation or automated feature identification (Gommes *et al.*, 2005; Batenburg & Sijbers, 2009; Friedrich *et al.*, 2009; Grothausmann *et al.*, 2011; Martínez-Sánchez *et al.*, 2011; Lebbink *et al.*, 2012; Fernández, 2013).

However, despite such advances in image acquisition and processing, the segmentation of a tomogram can still be a subjective and time-consuming procedure that can be affected by artefacts. In a previous study (Gontard, 2015), we demonstrated the importance of correcting the intensities of a tomographic series when a tilt series has an offset respect to the vacuum level due to the acquisition parameters used (i.e. gain and offset of the detector). If such an offset is not corrected then an *unreal material* that fulfils the 3D space degrades the fidelity of the tomographic reconstruction. Here, we extend the concept to *real materials* by showing how the application of a simple preprocessing step that involves downshifting the intensity level of each image in a tomographic tilt series until the contribution of low-density supporting material, embedding material or contamination layers is minimised or removed greatly reduces artefacts in tomograms, facilitating segmentation of the reconstructed 3D dataset.

## Materials and methods

When acquiring a tomographic tilt series of images using high-angle dark field scanning TEM (HAADF STEM) imaging, the lowest intensities in a histogram of each image may contain information from low-density and/or thin materials. We have previously shown that a tomographic reconstruction can contain artefacts and blurring when the images in a tilt series have an offset in their histograms (Gontard, 2015) and that, if the intensity of each image in a tilt series is downshifted after acquisition by an appropriate constant value, then the fidelity of the tomogram can be improved greatly. Here, we show that the same approach can be used as a thresholding procedure to minimise the contribution of layers of lower density material that are not of primary interest, resulting in improved fidelity of features of interest in a tomographic reconstruction.

We acquired tilt series of HAADF STEM images using a single tilt model 2020 tomography holder from Fischione Instruments and the Explore3D software package from FEI Company. Images were reconstructed using the multiplicative simultaneous iterative reconstruction technique (SIRT) algorithm. Visualisation and segmentation of the final 3D datasets was performed using Avizo software. Inspect 3D software uses a version of the .mrc file format (Crowther *et al.*, 1996). The images are saved in 16-bit *integer signed* format, meaning that pixel intensities take discrete values in the range  $-32\,678$  to  $+32\,677$  (Fig. 1D). This range of values is used for acquisition, storage and visualisation purposes. As a multiplicative SIRT algorithm ideally requires the intensities in a tilt series to be positive, with the vacuum intensity set to zero (Herman,

1979), we assume that for reconstruction the software rescales the image intensities internally so that they are unsigned.

We wrote a custom script using Matlab to read in and save tilt series of images in \*.mrc format and to downshift their intensities  $I(x, y, \theta)$ , so that

$$I(x, y, \theta) \rightarrow I(x, y, \theta) - K, \text{ for all } \theta,$$

where  $\theta$  is the tilt angle,  $x$  and  $y$  the pixel coordinates and  $K$  an offset that can in principle be different for each image, but is common to each image for simplicity in the examples shown below. The optimal value of  $K$  can be selected interactively by the user until the information in lower density areas is no longer present.

Thresholding methods are most effective when the histogram of an image is multimodal with well separated peaks (Bonnet *et al.*, 2002; González & Woods, 2002; Gommes *et al.*, 2005; Volkmann, 2010; Gontard *et al.*, 2011). Figure 1 illustrates the difference between thresholding a TEM image using the intensity downshifting approach proposed here (Fig. 1C) and conventional thresholding methods available for example in Inspect 3D software (Fig. 1D), which simply resets the pixels in an image that have intensities below a selected threshold value to zero. When the latter method is used, the layers of material above and/or below the particle are not removed from the images (see first and second row of Fig. 1D) because the sum of the intensities in the support/contamination layers and the intensities in the particle is above the threshold value. The projected thickness profile of the particle is then no longer correct.

A tilt series of HAADF STEM images of Pt particles was acquired between  $-75^\circ$  and  $+72^\circ$  with a  $1^\circ$  tilt increment, an acquisition time for each image of 15 s, using an FEI Tecnai F30 field emission gun TEM operated at 200 kV and a camera length corresponding to an inner detector semi-angle of  $\sim 50$  mrad to enhance the contrast between the cores and the shells of the particles, while minimising the effects of diffraction contrast. HAADF STEM electron tomography was also performed on a sample of amyloid plaque core material that had been suspended in PBS buffer, pipetted onto a Formvar film supported on a 200-mesh Cu grid (Agar Scientific Ltd., Essex, UK) and air-dried. Electron microscopy was performed immediately at 200 kV using an FEI Tecnai F20 ST field emission gun TEM. A tilt series of HAADF images was acquired over a tilt range of  $-70^\circ$  to  $+78^\circ$  using a  $2^\circ$  tilt increment and an acquisition time for each image of 40 s (Collingwood *et al.*, 2008).

## Results and discussion

### *Nanocatalysts supported on carbon black*

Figure 2(A) shows a representative HAADF STEM image acquired at  $0^\circ$  tilt taken from a tilt series of images of Pt nanoparticles supported on carbon black, which are used as a

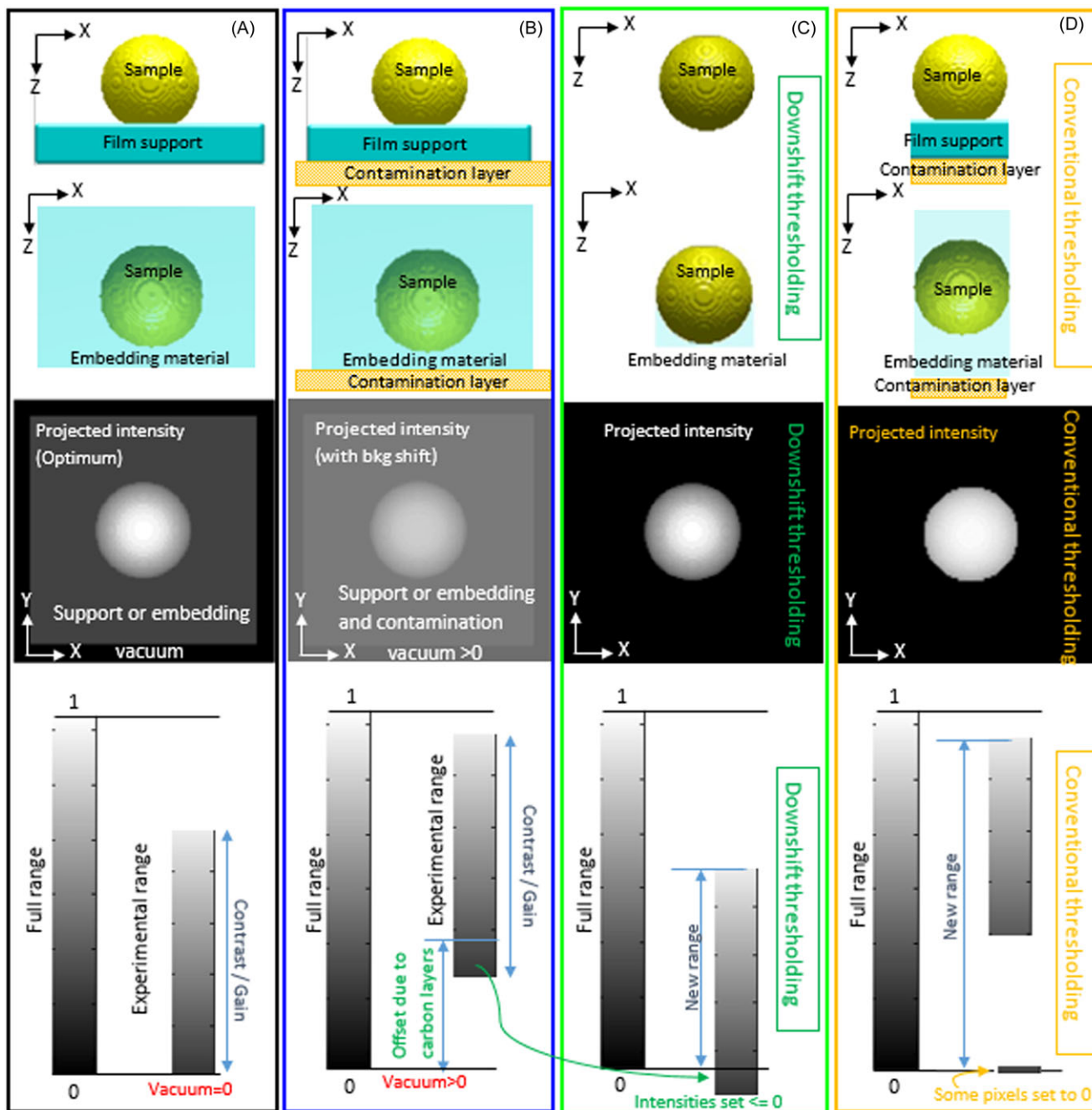
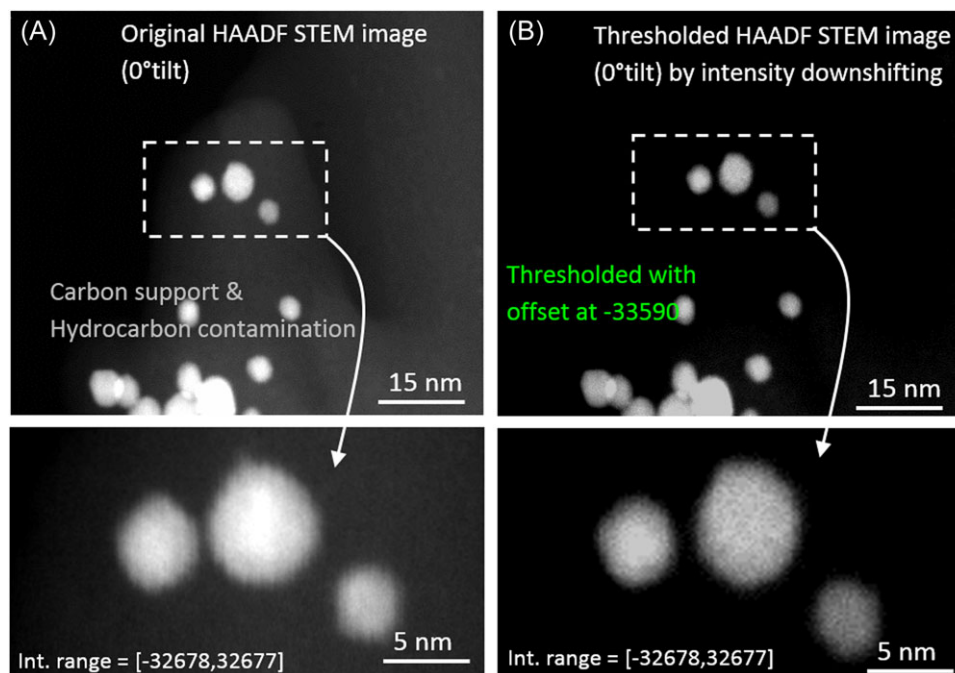


Fig. 1. Schematic diagrams illustrating thresholding of a low-density material. (A) The feature of interest is a single particle on a supporting film or surrounded by an embedding material. (B) The same than in (A) but surrounded also by carbonaceous contamination. (C) Proposed approach of thresholding and intensity downshifting. (D) Conventional method of thresholding by setting to zero all pixels with intensities below a predefined intensity.

heterogeneous catalyst (Gontard *et al.*, 2008). The aim of the study was to measure the shapes of the particles. As a result of the long acquisition time, hydrocarbon contamination built up during the tilt series. Although the use of a plasma cleaner before image acquisition can be used to minimise the build-up of contamination, this approach cannot be used

extensively when the sample itself is made of carbon. After the tilt series had been aligned, the intensities in the images were downshifted to a value of  $-33\,590$ , which was found to be sufficient to remove the carbon signal from most of the images in the tilt series, whereas the boundaries of the particles remained almost unchanged (Fig. 2B).



**Fig. 2.** Example of thresholding by intensity downshifting. (A) Representative HAADF STEM image recorded at  $0^\circ$  tilt taken from a tilt series of images of Pt nanoparticles supported on carbon black. The full tilt series was acquired at 200 kV using specimen tilt angles of between  $-75^\circ$  and  $+72^\circ$  with a tilt increment of  $1^\circ$ . Both a carbon support and carbonaceous contamination surround the particles. (B) The same image after adjusting the offset level to remove the signal from the carbon support and carbonaceous contamination. The lower images show magnified regions of the same areas (see also Fig. 4 below). The bottom figures correspond to the areas inside the dashed areas of the top row.

Figure 3(A) shows a comparison of histograms determined from tomograms obtained from both the original and the downshifted tilt series. After thresholding, the peak in the histogram at an intensity of  $-32\,678$  corresponds to voxels in the tomogram around the three Pt particles. In contrast, when using the original images, the histogram contains intensities to the left of the first peak, corresponding to voxels around the particles that blur their edges. Figure 3(B) shows central line profiles of intensities measured from the two tomograms. The line profiles confirm that the intensity of the background outside the particles is flat for the tomogram obtained from the thresholded tilt series.

Figures 3(C) and (D) show orthoslices (orthogonal planar slices) and both voltex and isosurface visualizations determined from the reconstructions before and after thresholding. Images have a pixel size of  $0.19$  nm. The reconstructed volume has a size of  $237 \times 154 \times 116$  voxels, and each slice has a thickness of only one voxel, and considering an elongation factor of 20% for a missing wedge of  $30^\circ$ , the voxel size in the projection direction (Z-direction) will be approximately between  $0.19$  and  $0.19 \times 1.2 = 0.228$  nm (Crowther *et al.*, 1970). When using the thresholded tilt series, blurring around the particles is almost absent, the influence of the missing wedge is minimised and

the particles can be segmented automatically without the need for manual intervention.

#### *Amyloid plaque core material*

Figure 4(A) shows a representative HAADF STEM image at  $0^\circ$  sample tilt taken from a tilt series of amyloid plaque core material extracted from human Alzheimer's disease (AD) brain tissue. The aim of the experiment was to study abnormal concentrations of Fe associated with the neurodegenerative disease (Collingwood *et al.*, 2008). The feature of interest is an Fe-rich core surrounded by an organic shell. The contrast in the image has been stretched to enhance low contrast features (the Fe-rich core is saturated). The image shows a ring of hydrocarbon contamination (arising because the area of interest was irradiated with a broad electron beam in TEM mode before acquisition of the tilt series) and additional scan lines that coincide with the direction of rastering of the electron beam.

Figure 4(B) shows the same image after thresholding the carbonaceous layer and downshifting the intensities in the image. Figure 4(C) shows central line profiles of intensities measured from the two images of the tilt series acquired at  $0^\circ$  tilt and shown in Figures 4(A) and 4(B). After downshifting the minimum level of intensity of the original image at an

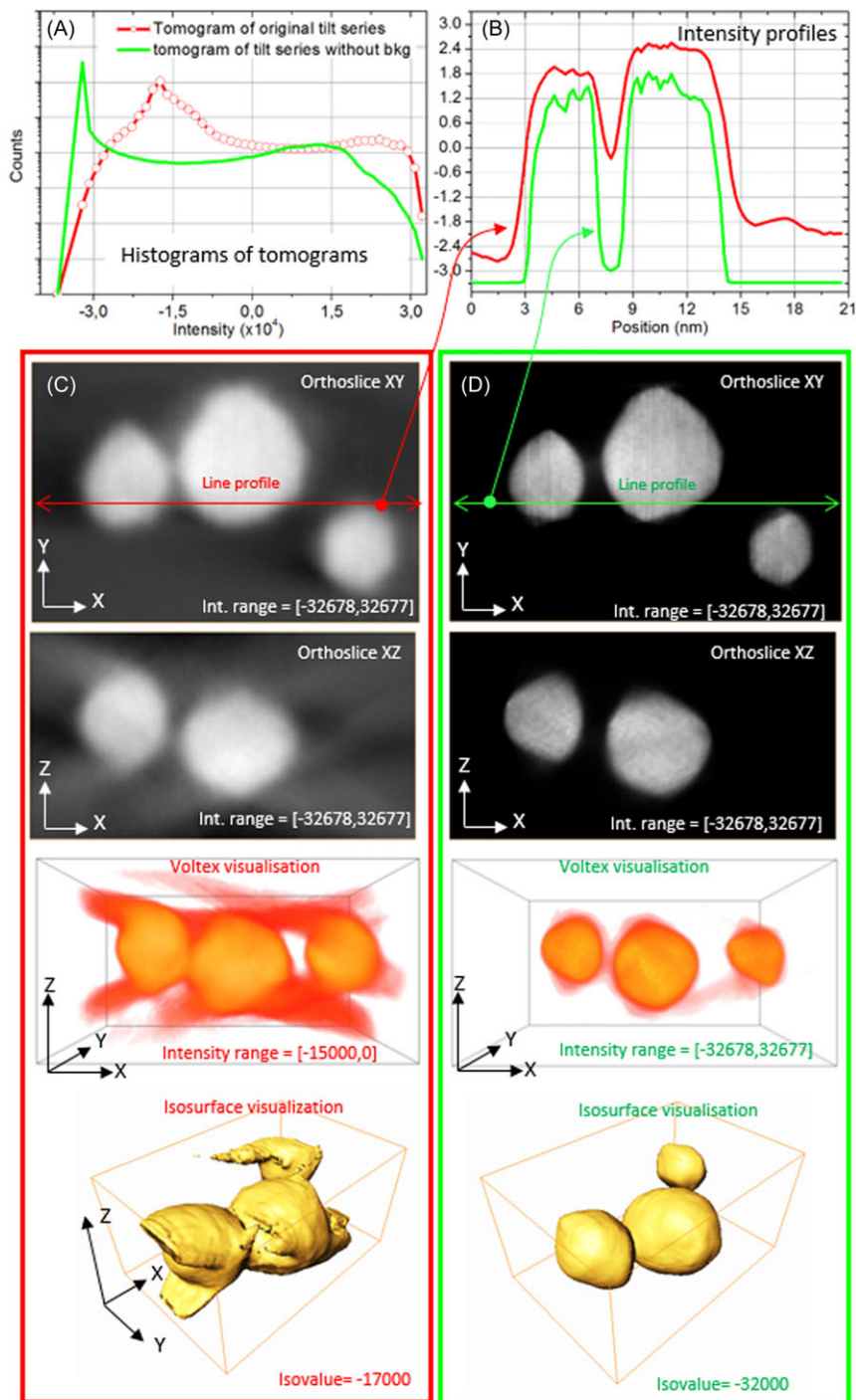


**Fig. 3.** Illustration of improvement in segmentation of tomograms after intensity downshifting. (A) Histograms of intensities in tomograms obtained from the HAADF STEM tilt series of Pt particles, from which images are shown in Figures 2(A) (red) and 2(B) (green). (B) Line profiles measured from XY orthoslices along the lines indicated. (C), (D) Show information obtained from tomograms calculated from the tilt series before and after thresholding and intensity downshifting. From top to bottom, the rows show orthoslices extracted from the tomograms in the XY and XZ planes, vortex visualisations and isosurface visualisations determined using an isosurface value of  $-17\,000$ . The images in (C) show streaking artefacts and blurring in the XZ plane resulting from the missing wedge and the difficulty of accurate segmentation. In the images shown in (D), the information about the carbon support and contamination layer is no longer available, but most of the artefacts have disappeared and segmentation of the Pt particles is more accurate. The orthoslices are displayed with the full dynamic range  $[-32\,678, 32\,677]$ , indicating that most artefacts in the tomogram are greatly reduced after thresholding.

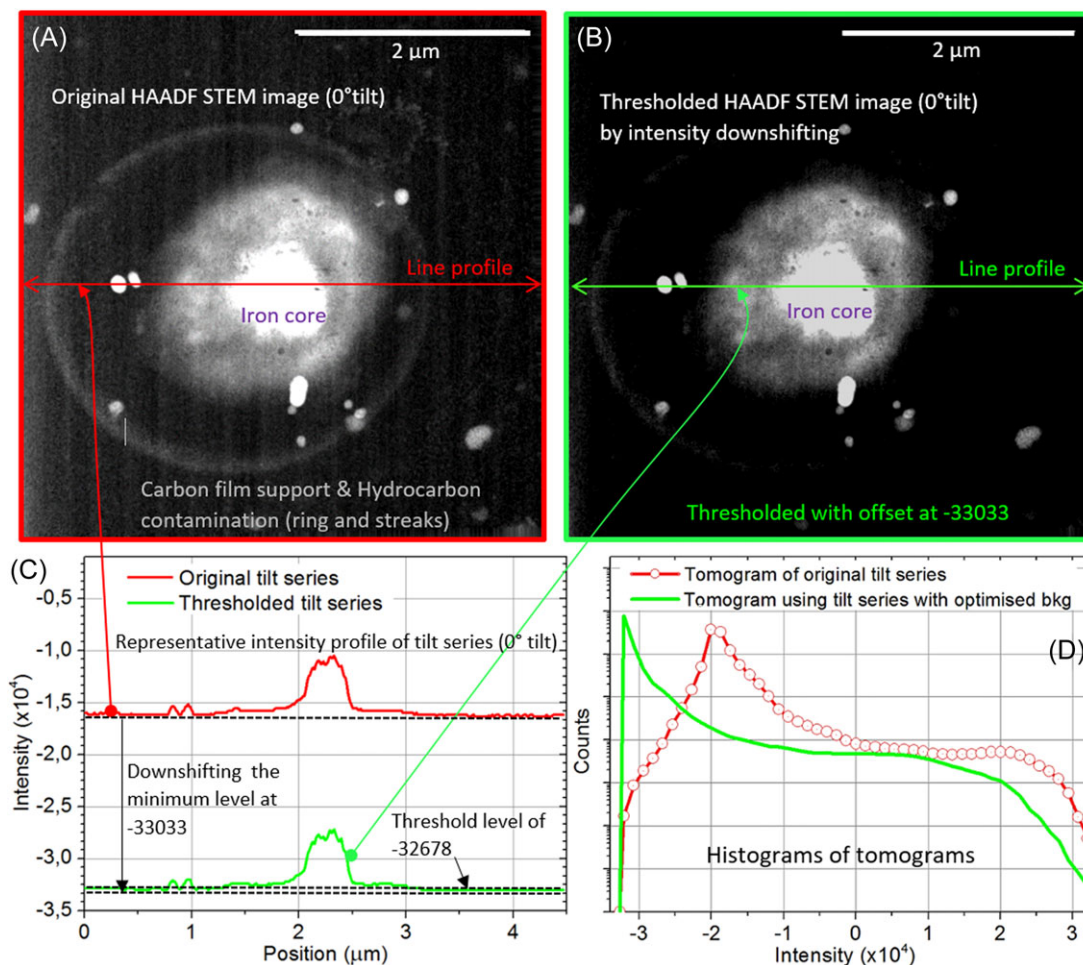


Fig. 4. Illustration of intensity downshifting. (A), (B) Representative HAADF STEM images recorded at 0° tilt taken from a tilt series of HAADF STEM images of amyloid plaque core material extracted from human AD brain tissue. The images are shown before and after thresholding and intensity downshifting, respectively, in order to minimize the influence of the signal from the carbon contamination and support film. (C) Shows central line profiles of intensities in the same images. (D) Shows histograms of intensities in tomograms determined from the tilt series before and after thresholding and intensity downshifting in red and green, respectively.

intensity level of  $-33033$ , all the pixels with intensities below the minimum level of an image with 16-bit *integer signed* format (i.e.  $-32678$ ) are thresholded. Figure 4(D) shows comparisons between histograms determined from the original images and the final tomograms, respectively. Just as in Figure 3, the peak in the histogram determined from the tomogram coincides with the minimum level of intensity and is indicative of less blurring and fewer artefacts after intensity downshifting.

When downshifting intensities, it is important to note that, in general, there will not be a single threshold value that removes the contribution of low-density material for each image in a tilt series, because the projected thickness of the low-density layers will change as the sample is tilted. If the threshold is not chosen carefully, then part of the signal of interest may be lost in some images. For example, in Figure

4(B), some information was lost as a result of intensity downshifting and the edge of the organic shell are slightly smaller than that in the original image shown in Figure 4(A). Such a possible loss of information is a compromise that should be taken into account when making quantitative measurements from tomograms, either before or after segmentation.

Nevertheless, Figures 5(A) and 5(B) show a significant improvement in the quality of the segmentation of the reconstructed tomogram before and after thresholding the carbon layers. Images have a pixel size of 9.5 nm. The reconstructed volume has a size of  $370 \times 350 \times 92$ , and each slice has a thickness of only one voxel, that is, a thickness between 9.5 and below 11.4 nm (considering that the elongation factor is about 20%). The most evident improvement is the disappearance of artefacts associated with the missing wedge, which are clearly visible in Figure 5(A).

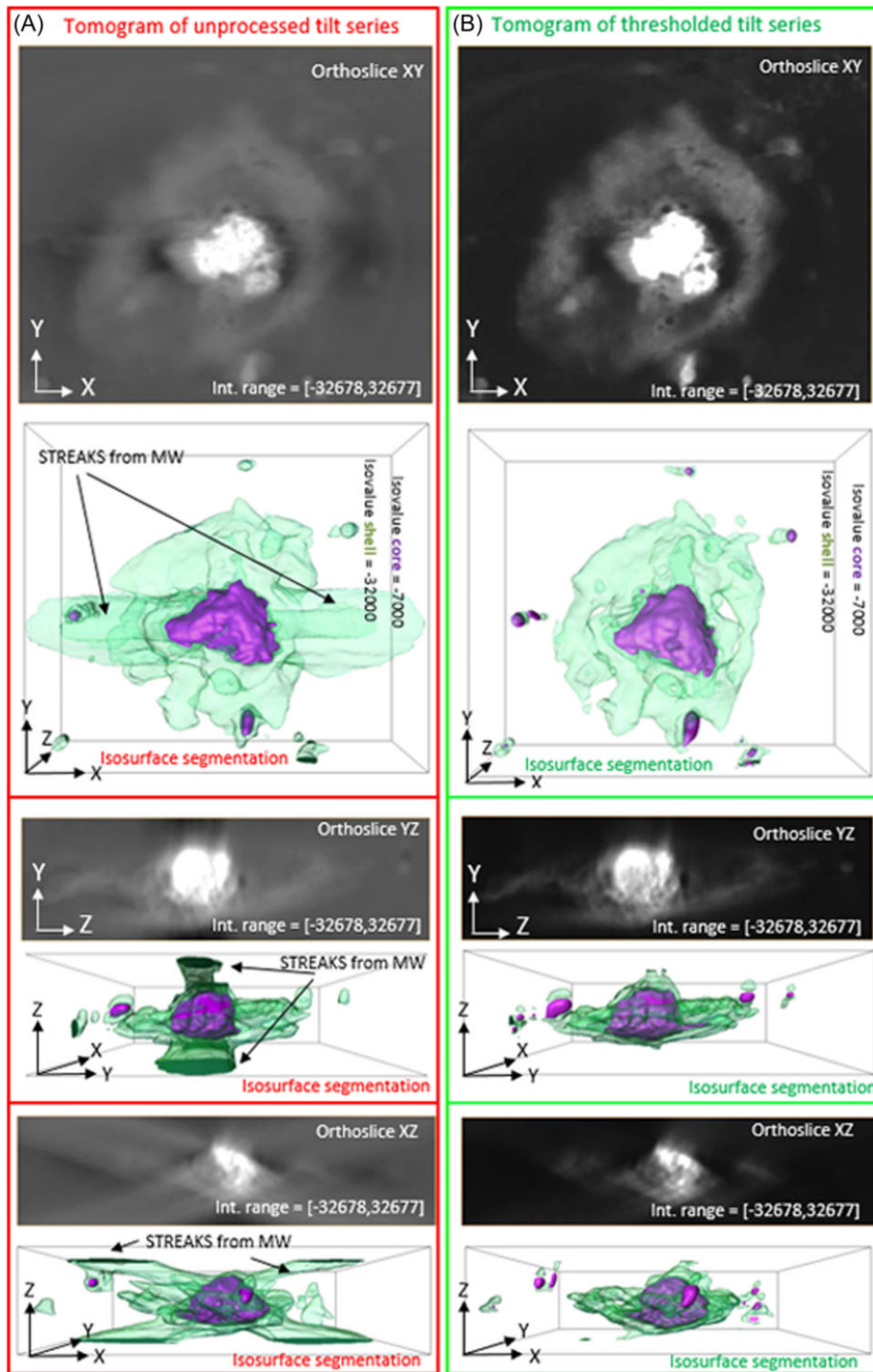


Fig. 5. Illustration of improvement in segmentation of tomograms after intensity downshifting. (A), (B) Show information obtained from tomograms of the samples shown in Figure 4 before and after thresholding and intensity downshifting, respectively. The rows show orthoslices extracted from the tomograms in the XY and XZ planes, vortex visualisations and isosurface visualisations determined using an isosurface value of the tomograms parallel to the XY and YZ planes and isosurface visualisations. Segmentation of the Fe cores and C-based shells was performed using the indicated isosurface values. The orthoslices are displayed with the full dynamic range  $[-32\ 678, 32\ 677]$ , indicating that most artefacts are greatly reduced from the tomogram after thresholding.

## Conclusions

Segmentation is widely used to extract morphological information from electron tomograms. However, the presence of embedding material, a thin film support or electron-beam-induced contamination can introduce artefacts around features of interest and complicate segmentation and interpretation of tomographic reconstructions. Here, we show that a simple downshifting of intensities in images in a tomographic tilt series by a constant value, in order to minimize or eliminate the influence of low-density materials that are not part of the signal of interest, can be used as a preprocessing step to greatly improve the fidelity of a tomogram and facilitate segmentation. For many samples, the method provides improved results of a final tomographic reconstruction when compared with unprocessed tomograms or with conventional thresholding, in particular when using a multiplicative iterative algorithm to perform a reconstruction from an HAADF-STEM tilt series of images.

## Acknowledgements

The authors wish to thank Dogan Ozkaya, Ryan K.K Chong, Joanna Collinwood and Jon Dobson for the provision of samples and for their involvement in the experiments. The research leading to these results has received funding from the European Union Seventh Framework Programme under Grant Agreement 312483 - ESTEEM2 (Integrated Infrastructure Initiative-13).

## References

- Alpers, A., Gardner, R.J., König, S., Pennington, R.S., Boothroyd, C.B., Houben, L., Dunin-Borkowski, R.E. & Batenburg, K.J. (2013) Geometric reconstruction methods for electron tomography. *Ultramicroscopy* **128**, 42–54.
- Bals, S., Casavola, M., van Huis, M.A., Van Aert, S., Batenburg, K.J., Van Tendeloo, G. & Vanmaekelbergh, D. (2011) Three-dimensional atomic imaging of colloidal core-shell nanocrystals. *Nano Lett.* **11**, 3420–3424.
- Batenburg, K.J., Bals, S., Sijbers, J. *et al.* (2009) 3D imaging of nanomaterials by discrete tomography. *Ultramicroscopy* **109**, 730–740.
- Batenburg, K.J. & Sijbers, J. (2009) Adaptive thresholding of tomograms by projection distance minimization. *Patt. Recogn.* **42**, 2297–2305.
- Bonnet, N., Cutron, J. & Herbin, M. (2002) A ‘no-threshold’ histogram-based image segmentation method. *Patt. Recogn.* **35**, 2319–2322.
- Cao, M., Zhang, H.-B., Lu, Y., Nishi, R. & Takaoka, A. (2010) Formation and reduction of streak artefacts in electron tomography. *J. Microsc.* **239**(1), 66–71.
- Collingwood, J.F., Chong, R.K.K., Kasama, T. *et al.* (2008) Three-dimensional tomographic imaging and characterization of iron compounds within Alzheimer’s plaque core material. *J. Alzh. Dis.* **14**, 235–245.
- Crowther, R.A., Henderson, R., Smith, J.M. (1996) MRC image processing programs. *J. Struct. Biol.* **116**(1), 9–16.
- Crowther, R.A., de Rosier, D.J. & Klug, A. (1970) The reconstruction of a three-dimensional structure from projections and its application to electron microscopy. *Proc. R. Soc. Lond.* **A319**, 317–340.
- Fernández, J.J. & Li, S. (2003) An improved algorithm for anisotropic nonlinear diffusion for denoising cryo-tomograms. *J. Struct. Biol.* **144**, 152–161.
- Fernández, J.J., Sorzano, C.O.S., Marabini, R. & Carazo, J.M. (2006) Image processing and 3-D reconstruction in electron microscopy. *IEEE Signal Process. Mag.* **23**(3), 84–94.
- Fernández, J.-J. (2013) Computational methods for materials characterization by electron tomography. *Curr. Opin. Solid State Mater. Sci.* **17**, 93–105.
- Frangakis, A. & Hegerl, R. (2001) Noise reduction in electron tomographic reconstructions using nonlinear anisotropic diffusion. *J. Struct. Biol.* **135**, 239–250.
- Friedrich, H., de Jongh, P.E., Verkleij, A.J. & de Jong, K.P. (2009) Electron tomography for heterogeneous catalysts and related nanostructured materials. *Chem. Rev.* **109**(5), 1613–1629.
- Gommes, C.J., de Jong, K., Pirard, J.-P. & Blacher, S. (2005) Assessment of the 3D Localization of metallic nanoparticles in Pd/SiO<sub>2</sub> cogelled catalysts by electron tomography. *Langmuir* **21**, 12378–12385.
- Gontard, L.C., Dunin-Borkowski, R.E. & Ozkaya, D. (2008) Three-dimensional shapes and spatial distributions of Pt and PtCr catalyst nanoparticles on carbon black. *J. Microsc.* **232**(2), 248–259.
- Gontard, L.C., Ozkaya, D. & Dunin-Borkowski, R.E. (2011) A simple algorithm for measuring particle size distributions on an uneven background from TEM images. *Ultramicroscopy* **111**, 101–106.
- Gontard, L.C., Knappett, B.R., Wheatley, A.E.H., Chang, S.L.-Y. & Fernández, A. (2014) Impregnation of carbon black for the examination of colloids using TEM. *Carbon* **76**, 464–468.
- Gontard, L.C. (2015) Removing the effects of the ‘dark matter’ in tomography. *Ultramicroscopy* **154**, 64–72.
- González, R.C. & Woods, R.E. (2002) *Digital Image Processing*, 2 edn. Prentice Hall, Upper Saddle River, New Jersey.
- González, J.C., Hernández, J.C. *et al.* (2009) 3D characterization of gold nanoparticles supported on heavy metal oxide catalysts by HAADF-STEM electron tomography. *Angew. Chem. Int. Ed.* **48**, 5313–5315.
- Goris, B., Van den Broek, W., Batenburg, K.J., Mezerji, H.H. & Bals, S. (2012) Electron tomography based on a total variation minimization reconstruction technique. *Ultramicroscopy* **113**, 120–130.
- Grimm, R., Singh, H., Rachel, R., Typke, D., Zillig, W. & Baumeister, W. (1998) Electron tomography of ice-embedded prokaryotic cells. *Biophys. J.* **74**, 1031–1042.
- Grothausmann, R., Zehl, G., Manke, I. *et al.* (2011) Quantitative structural assessment of heterogeneous catalysts by electron tomography. *J. Am. Chem. Soc.* **133**, 18161–18171.
- Herman, G.T. (1979) *Image Reconstruction from Projections: Implementation and Applications*, Topics in Applied Physics, 32. Springer-Verlag, Berlin, Germany.
- Jarausch, K. & Leonard, D.N. (2009) Three-dimensional electron microscopy of individual nanoparticles. *J. Electr. Microsc.* **58**(3), 175–183.
- Jinschek, J.R., Batenburg, K.J., Calderon, H.A., Kilaas, R., Radmilovic, V. & Kisielowski, C. (2008) 3-D reconstruction of the atomic positions in a simulated gold nanocrystal based on discrete tomography: prospects of atomic resolution electron tomography. *Ultramicroscopy* **108**, 589–604.
- Koster, A.J., Ziese, U., Verkleij, A.J., Janssen, A.H. & de Jong, K.P. (2000) Three-dimensional transmission electron microscopy: a novel imaging and characterization technique with nanometer scale resolution for materials science. *J. Phys. Chem. B.* **104**, 9368–9370.

- Lange, A., Kupsch, A., Hentschel, M.P., Manke, I., Kardjilov, N., Arlt, T. & Grothausmann, R. (2011) Reconstruction of limited computed tomography data of fuel cell components using direct iterative reconstruction of computed tomography trajectories. *J. Pow. Sour.* **196**, 5293–5298.
- Leary, R., Saghi, Z., Midgley, P.A. & Holland, D. J. (2013) Compressed sensing electron tomography. *Ultramicroscopy*. **131**, 70–91.
- Lebbink, M.N., Hekking, L.H.P., Geerts, W.J.C. & Post, J.A. (2012) D-CAT: density and clustering annotation tool for three dimensional electron microscopic volumes. *J. Struct. Biol.* **177**, 571–577.
- Leschner, J., Biskupek, J., Chuvilin, A. & Kaiser, U. (2010) Accessing the local three-dimensional structure of carbon materials sensitive to an electron beam. *Carbon*. **48**, 4042–4048.
- Martinez-Sanchez, A., Garcia, I. & Fernandez, J.J. (2011) A differential structure approach to membrane segmentation in electron tomography. *J. Struct. Biol.* **175**, 372–383.
- Midgley, P.A. & Weyland, M. (2003) 3D electron microscopy in the physical sciences: the development of Z-contrast and EFTEM tomography. *Ultramicroscopy*. **96**, 413–431.
- Midgley, P.A. & Dunin-Borkowski, R.E. (2009) Electron tomography and holography in materials science. *Nat. Mater.* **8**, 271–280.
- Ortalan, V., Herrera, M., Morgan, D.G. & Browning, N.D. (2009) Application of image processing to STEM tomography of low-contrast materials. *Ultramicroscopy*. **110**, 67–81.
- Reimer L. & Kohl, H. (2008) *Transmission Electron Microscopy, Physics of Image Formation*, 5th edn, pp. 484–486. Springer, New York.
- Roelandts, T., Batenburg, K.J., Biermans, E., Kübel, C., Bals, S. & Sijbers, J. (2012) Accurate segmentation of dense nanoparticles by partially discrete electron tomography. *Ultramicroscopy*. **114**, 96–105.
- Scott, M.C., Chen, C.C., Mecklenburg, M. *et al.* (2012) Electron tomography at 2.4-Ångström resolution. *Nature*. **483**, 444–448.
- Tong, J., Arslan, I. & Midgley, P. (2006) A novel dual-axis iterative algorithm for electron tomography. *J. Struct. Biol.* **153**, 55–63.
- Van den Broek, W., Rosenauer, A., Van Aert, S., Sijbers, J. & Van Dyck, D. (2014) A memory efficient method for fully three-dimensional object reconstruction with HAADF STEM. *Ultramicroscopy*. **141**, 22–31.
- Van den Broek, W., Rosenauer, A., Goris, B., Martinez, G.T., Bals, S., Van Aert, S. & Van Dyck, D. (2012) Correction of non-linear thickness effects in HAADF STEM electron tomography. *Ultramicroscopy*. **116**, 8–12.
- Volkman, N. (2010) Methods for segmentation and interpretation of electron tomographic reconstructions. *Method. Enzymol.* **483**, 31–46.